ChemComm

Accepted Manuscript

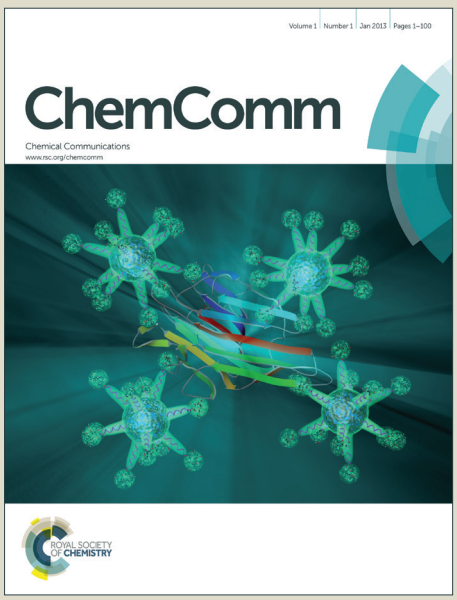

ROYAL SOCIETY OF CHEMISTRY

www.rsc.org/chemcomm

ChemComm

COMMUNICATION

$CoTe_2$ nanostructure: An efficient and robust catalyst for hydrogen evolution

Received 00th January 20xx,
Accepted 00th January 20xx

DOI: 10.1039/x0xx00000x

www.rsc.org/

Tzu-Hsiang Lu,[a] Chih-Jung Chen,[a] Mrinmoyee Basu,[a] Chong-Geng Ma[b], and Ru-Shi Liu*[ac]

Cobalt ditelluride nanoparticles with a diameter range of 20–50 nm were sythesized as a new electrocatalyst for the hydrogen evolution reaction in 0.50 M $H_2SO_{4(aq)}$. These nanoparticles can generate −10 mA/cm^2 at an overpotential of 246 mV without any decay up to 48 h of continuous reaction.

Energy crisis and environmental issues have continuously increased in recent years. Hydrogen as clean fuel is a promising energy carrier in hydrogen economy paradigm[1] because of its large mass storage density and long storage time[2]. Electrochemical reduction of water is a simple method for hydrogen production. Pt-based catalysts exhibit high performance for the hydrogen evolution reaction (HER), which reduces protons to molecular hydrogen (H_2) in acidic solutions[3]; however, Pt is an expensive noble metal[4]. Therefore, low cost and stable catalysts with a high current density must be developed for HER at low overpotentials. As an alternative to Pt, earth-abundant elements have been used to develop new less expensive acid-stable catalysts, such as MoS_2[5], CoS_2[6], WS_2[7], $CoSe_2$[8], W_2N[9], $NiMoN_X$[10], CoP[11], FeP[12], Ni_2P[13], WP[14], Mo_2C[15], WC[16], and MoB[17]. Cobalt is an interesting non-noble metal because of its catalytic power toward hydrogen evolution. In this regard, scholars have focused on the development of Co-based complexes as HER catalysts. First-row transition-metal dichalcogenides (ME_2, M = Fe, Co, Ni; E = S, Se) have also been studied as active electrocatalysts for the oxygen reduction reaction in acidic electrolytes[18]. The high activity of dichalcogenides for HER has been recently confirmed[19]. Dai et al. indicated that anion is the active site of dichalcogenides for HER[20]. This study also showed that electrocatalytic activity is strongly dependent on the adsorption strength of the hydrogen to the active site. If the adsorption strength is large, electrocatalytic activity is low because of the weak desorption of H_2. As such, we predict that $CoTe_2$ presents low adsorption strength for H_2 because of the low electronegativity of Te and thus exhibits electrocatalytic activity toward HER. In the composition range of Co:Te = 1:1–1:2, two different phases exist, which include trigonal CdI_2-type and orthorhombic marcasite-type [21], with the latter as more stable. The present study is the first to introduce orthorhombic marcasite-type $CoTe_2$ as an electrocatalysts for HER. Hydrothermal method was used to synthesize $CoTe_2$, and $CoTe_2$ ink was subsequently prepared by dropping ethanol and Nafion on the rotating ring-disk electrode (RRDE). $CoTe_2$ nanoparticles (NPs) exhibit efficient electrocatalytic activity in acid solutions, with an onset potential (η) of 198 mV and a Tafel slope of 45.9 mV/dec. $CoTe_2$ requires overpotentials of 217 and 246 mV to produce −2 and −10 mA/cm^2, respectively, and maintain electrocatalytic activity for 48 h. The $CoTe_2$ catalyst for HER shows high performance with high stability in acid solutions.

Centrifugation was then performed to separate $CoTe_2$ NPs and microsheets (MSs). The X-ray diffraction (XRD) pattern shows the diffraction peak of $CoTe_2$ NPs and MSs (Fig. 1). The strong peak observed at 21.8°, 26.8°, 28.3°, 31.7°, 32.9°, 33.6°, 43.5°, 46.5°, 49.1°, and 58.2 can be indexed with the Miller indices (110), (011), (101), (111), (120), (200), (211), (002), (031), and (122), respectively. These peaks correspond to the characteristic diffraction peaks of the orthorhombic macarsite mattagamite (JCPDS-89-2091) (Fig. S1). The peak of $CoTe_2$ MSs is not sharper than that of $CoTe_2$ NPs, which indicates that the primary particle size of $CoTe_2$ NPs is similar to that of $CoTe_2$ MSs. A small amount of TeO_2 impurity phase was also observed. The transmission electron microscopy (TEM) images of

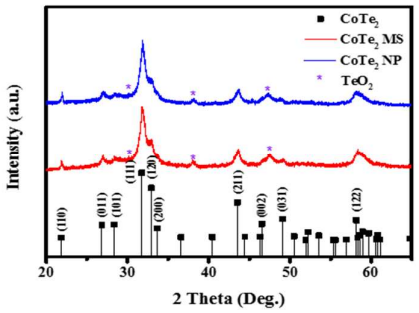

Fig. 1 Structural characterization of $CoTe_2$ NPs and MSs. XRD patterns of $CoTe_2$ NPs and MSs

NPs and MSs (Fig. 2a and 2b) show that their secondary diameter sizes are 20–50 and 200–400 nm, respectively. The TEM images also reveal the hexagonal MSs and NPs of $CoTe_2$. Moreover, the low-magnification scanning electron microscopy (SEM) images further indicate the morphology of $CoTe_2$ NPs and $CoTe_2$ MSs (Figs. S2a and S2b, ESI). The high-magnification SEM images show that

[a] Department of Chemistry, National Taiwan University, Taipei 10617, Taiwan. E-mail : rsliu@ntu.edu.tw
[b] College of Sciences, Chongqing University of Posts and Telecommunications, Chongqing 400065, China
[c] Department of Mechanical Engineering and Graduate Institute of Manufacturing Technology, National Taipei University of Technology, Taipei 10608, Taiwan.
† Electronic Supplementary Information (ESI) available: Full experimental details and additional data (). See DOI: 10.1039/x0xx00000x

numerous MSs and NPs are interconnected with each other (Figs. S2c and S2d, ESI).

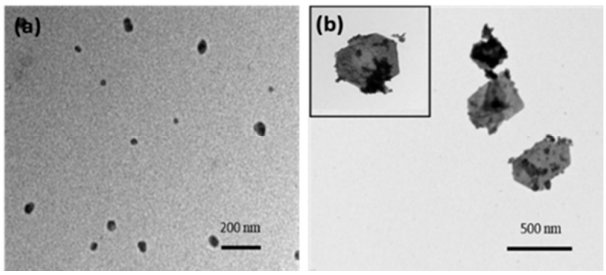

Fig. 2 TEM images of (a) $CoTe_2$ NPs and (b) MSs.

The composition of $CoTe_2$ NPs and MSs was determined by energy-dispersive X-ray (EDX; Figs. S3a and S3b, ESI) and inductively coupled plasma-mass spectroscopy (ICP-mass; Figs. S4a and S4b, ESI). The measured atomic ratios of Co to Te are about 1:2.05 and 1:2.20 based on the EDX (Table S1a and S1b, ESI) and ICP-mass results (Tables S2a and S2b, ESI). We propose that TeO_2 is partially generated on the surface during the hydrothermal reaction because the ratio of Co and Te is slightly higher than 2. Nevertheless, TeO_2 dissolves in acid solutions during HER measurements and is inert toward the electrochemical activity of $CoTe_2$ materials[22]. As such, the chemical state of the Co ions in $CoTe_2$ was experimentally checked by Co K-edge X-ray absorption near edge structure (XANES) (Fig. 3). Co foil (Co with zero charge), CoO (Co with 2^+ charge), Co_3O_4 (Co with mixed 2^+ and 3^+ charges), and Co_2O_3 (Co with 3^+ charge) were used as standard materials. A chemical negative shift was observed in the Co K-edge jump for $CoTe_2$, similar to the negative Co K-edge jump of CoS_2 (pyrite) with respect to CoO[23]. This phenomenon is attributed to the lower electronegativity of Te than that of O. Although the Co K-edge absorption of $CoTe_2$ was determined between the Co foil and CoO, the chemical state of Co in $CoTe_2$ is Co^{2+}; hence, the form of Te in $CoTe_2$ should be Te_2^{2-}. $CoTe_2$ is regarded as the sum of Co^{2+} and Te_2^{2-} from the ionic perspective, and this phenomenon is confirmed by the Mulliken charge analysis of our first-principles calculation (Table S3, ESI). The band structure and partial and total densities of

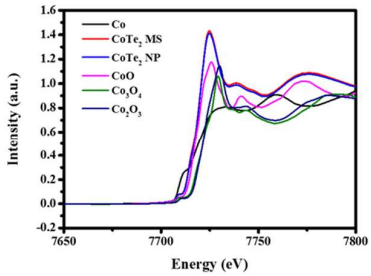

Fig. 3 XANES spectra of $CoTe_2$ and the oxide standards containing Co.

states (PDOS/DOS) diagrams for $CoTe_2$ was theoretically calculated (Figs. S5 and S6, ESI). The half-metallic nature can be easily concluded from the calculated position of the Fermi energy level E_F, and the mechanism underlying such formation is provided in our previous work on $CoSe_2$[24]. The band structure for inorganic electrocatalysts near the Fermi level is dependent on the adsorption strength of the reactants[25]. The optimal band structure to obtain high HER activity is the partially filled bands. The band gap for beta electrons (with down spin) in $CoTe_2$ is indirect (*SM*→*LD*) and equal to 1.063 eV. Comparison between $CoTe_2$ and $CoSe_2$ reveals that the 3d CF splitting between the t_{2g} and e_g states for beta electrons in $CoTe_2$ is smaller because of longer Co–Te interionic distances. In addition, the Co-Te chemical bonding should be more covalent because of the strong hybridization between the Co-3*d* and Te-5*p* states, as shown in the DOS diagrams.

All measurements of HER activity were performed in 0.5 M $H_2SO_{4(aq)}$ electrolyte solution. The original polarization curve can be obtained using linear sweep voltammetry (LSV) (Fig. S7, ESI). The Nyquist plots of $CoTe_2$ NPs and MSs were measured at potentials of −0.20 and −0.30 V (near the onset potential) through electrochemical impedance spectroscopy (EIS). The experimental data was then fitted to the electrical model (Fig. 4a). The R_s of $CoTe_2$ NPs indicates an overall series resistance of 0.84 ohm cm^2, whereas R_{ct} represents the charge transfer resistance at the $CoTe_2$/electrolyte interface (1.41 ohm·cm^2). Compared with those of $CoTe_2$ NPs, the R_s and R_{ct} values of $CoTe_2$ MSs are 1.46 and 2.86 ohm·cm^2, respectively. The R_{ct} of $CoTe_2$ NPs is lower than that of $CoTe_2$ MSs; hence, $CoTe_2$ NPs exhibits higher efficiency for HER because electrons can rapidly transfer to the electrolyte. Nevertheless, the measured cathodic current could not present the original behavior of the catalysts because of the ohmic resistance effect. As such, iR loss was corrected to the initial data of the cathodic current and the background was removed (Fig. S8, ESI). After obtaining the EIS data, the polarization curves present the current density plotted against the applied potential, which were corrected for background removal and iR loss (Fig. 4b). The origin of the background current is complex and possibly caused by capacitive charging of the $CoTe_2$ surface[6]. The current density of $CoTe_2$ NPs rapidly increases with further negative potential scans; thus, overpotentials of 217 and 246 mV are required to produce current densities of −2 and −10 mA/cm^2. By contrast, $CoTe_2$ MSs require overpotentials of 294 and 330 mV to produce current densities of −2 and −10 mA/cm^2. Pt/C (20%) could drive −10 mA/cm^2 at an overpotential of 10 mV. A two-electron reaction can be used to distinguish two kinds of mechanism through two steps[26]. The first step is the discharge step (Volmer reaction: $H_3O^+ + e^- \rightarrow H_{ads} + H_2O$), followed by the desorption step (Heyrovsky reaction: $H_{ads} + H_3O^+ + e^- \rightarrow H_2 + H_2O$)

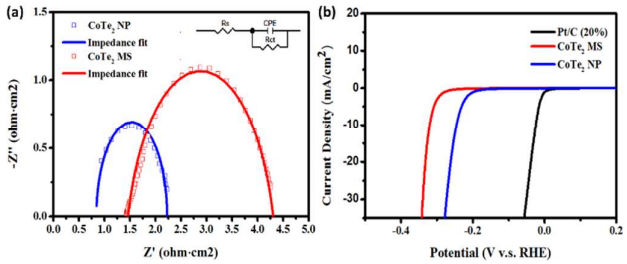

Fig. 4 (a) EIS Nyquist plots of the series and charge transfer resistance. (b) Polarization curves show the relative performance of the $CoTe_2$ electrodes compared with Pt/C (20%).

or the recombination step (Tafel reaction: $H_{ads} + H_{ads} \rightarrow H_2$). H_{ads} represents an H atom adsorbed at the active catalyst site. The rate-determining step in the HER mechanism could be Volmer, Heyrovsky, or Tafel reaction with Tafel slopes of 29, 38, and 116 mV/decade. The Tafel plots (log | j | vs. E) of $CoTe_2$ NPs and MSs show that the Tafel slopes are located near the onset of current densities of 45.9 and 41.0 mV/decade (Fig. 5), whereas the Tafel slope of Pt/C (20%) is 30.3 mV/decade. The Tafel slopes of $CoTe_2$ NPs and MSs do not match the expected Tafel slopes of 29, 38, and 116 mV/dec; as such, the Volmer–Heyrovsky reaction pathway with desorption reaction is the possible rate-limiting step of HER. The onset potential was also determined from the start of the linear part of the Tafel plot. $CoTe_2$ NPs, which were used as an efficient HER cathode, present an onset potential of −198 mV based on the linear part in the Tafel plot, whereas $CoTe_2$ MS demonstrate an onset

potential of −272 mV. The exchange current density can be typically extracted from the Tafel plot and applied to be proportional to the catalytically active surface area. The exchange current density of $CoTe_2$ NPs is about 5.9×10^{-5} A/cm^2, which is about three orders of magnitude higher than the value of 9.9×10^{-8} A/cm^2 for $CoTe_2$ MSs. The active surface area can also be estimated using C_{dl} at the solid–liquid interface through cyclic voltammetry (CV) measurements (Figs. S9a and S9b)[27]. The C_{dl} values of $CoTe_2$ NPs and MSs are 26.7 and 4.15 mF/cm^2, respectively (Figs. S9c and S9d, ESI). This finding indicates that more active sites exist in $CoTe_2$ NPs than that in $CoTe_2$ MPs, which results in lower overpotential requirements for $CoTe_2$ NPs.

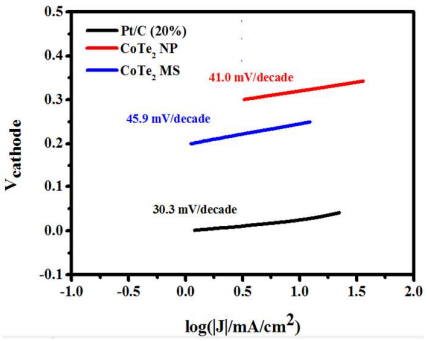

Fig. 5 Tafel plots show the HER mechanism of the $CoTe_2$ electrodes compared with Pt/C (20%).

In addition to high current density, stability is another important factor for the development of electrocatalysts. The durability of the synthesized $CoTe_2$ was examined by measuring continuous CV with a scanning rate of 100 mV for 1000 cycles. The polarization curves (corrected) after 1000 cycles almost overlap with the initial curves (Figs. S10a and S10b, ESI). The overpotential driven by a cathodic current of −10 mA/cm^2 exhibits cathodic shifts of 4 mV for $CoTe_2$ NPs and 5 mV for $CoTe_2$ MSs. Time-dependent potentiostatic electrolysis experiment at an overpotential-driven cathodic current of −10 mA/cm^2 was processed within 48 h (Figs. 5a and 5b). The results show that current density does not evidently decay within the processing period. The orthorhombic $CoSe_2$ (marcasite) was prepare to compare the activity with $CoTe_2$. The XRD pattern was corresponded to JCPDS-89-2003 (Fig. S11). Although the overpotential of $CoTe_2$ is higher than marcasite $CoSe_2$ (218 mV at -10mA/cm^2) but the stability of marcasite $CoSe_2$ is not really high enough (Fig. S12a). In time-dependent potentiostatic electrolysis experiment, current density of $CoSe_2$ decays about 80% at -246 mV within 6 h (Fig. S12b). This result depicts that $CoTe_2$ is much more eligible for practical application of H_2 evolution compared to $CoSe_2$.

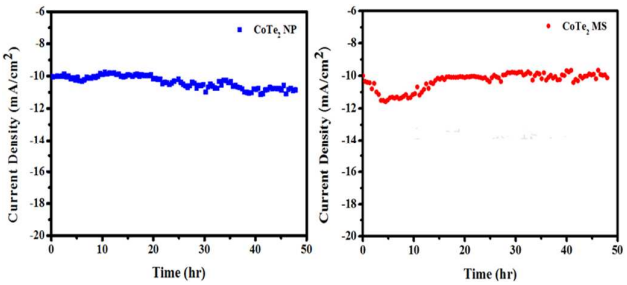

Fig. 6 Time dependence of cathodic current density for (a) $CoTe_2$ NPs and (b) $CoTe_2$ MSs for 48 h at fixed overpotentials of −246 and −330 mV.

In conclusion, we developed a simple hydrothermal method to fabricate $CoTe_2$ NPs and MSs. $CoTe_2$ NPs provided higher catalytic activity for HER than $CoTe_2$ MSs because NPs contain more active sites at a low morphology scale. The $CoTe_2$ NP catalyst coated on the RRDE exhibited high performance for HER with a small Tafel slope, large cathodic current at low overpotentials, and stability for more than 2 days. This novel material can be used in technological devices for solar water splitting.

This work was financially supported by the Ministry of Science, Technology of Taiwan (Contract No. MOST 104-2113-M-002-012-MY3 and Academia Sinica (Contract No. AS-103-TP-A06). C. G. Ma would also like to acknowledge the financial support from the National Natural Science Foundation of China (Grant No. 11204393). We are grateful for Ms. Chia-Ying Chien of the Instrumentation Center, National Taiwan University for performing the TEM experiments.

Notes and references

1 D. A. J. Rand and R. M. Dell, *Hydrogen Energy: Challenges and Prospects*, The Royal Society of Chemistry, 2007.
2 (a) J. A. Turner, *Science*, 2004, **305**, 972.
(b) H. B. Gray, *Nat. Chem*., 2009, **1**, 7.
3 (a) M. G. Walter, E. L. Warren, J. R. McKone, S. W. Boettcher, Q. Mi, E. A. Santori and N. S. Lewis, *Chem. Rev*., 2010, **110**, 6446.
(b) B. C. H. Steele and A. Heinzel, *Nature*, 2001, **414**, 345.
4 P. C. K. Vesborg and T. F. Jaramillo, *RSC Adv*., 2012, **2**, 7933.
5 (a) B. Hinnemann, P. G. Moses, J. Bonde, K. P. Jørgensen, J. H. Nielsen, S. Horch, I. Chorkendorff and J. K. Nørskov, *J. Am. Chem. Soc*., 2005, **127**, 5308.
(b) T. F. Jaramillo, K. P. Jørgensen, J. Bonde, J. H. Nielsen, S. Horch and I. Chorkendorff, *Science*, 2007, **317**, 100.
(c) Y. Li, H. Wang, L. Xie, Y. Liang, G. Hong and H. Dai, *J. Am. Chem. Soc*., 2011, **133**, 7296.
(d) Z. Chen, D. Cummins, B. N. Reinecke, E. Clark, M. K. Sunkara and T. F. Jaramillo, *Nano Lett*. 2011, **11**, 4168.
(e) D. Merki, H. Vrubel, L. Rovelli, S. Fierro and X. Hu, *Chem. Sci*., 2012, **3**, 2515.
(f) J. Kibsgaard, Z. Chen, B. N. Reinecke and T. F. Jaramillo, *Nat. Mater*., 2012, **11**, 963.
(g) M. A. Lukowski, A. S. Daniel, F. Meng, A. Forticaux, L. Li and S. Jin, *J. Am. Chem. Soc*., 2013, **135**, 10274.
(h) D. Merki, S. Fierro, H. Vrubel and X. Hu, *Chem. Sci*. 2011, **2**, 1262.
(i) Y. H. Chang, C. T. Lin, T. Y. Chen, C. L. Hsu, Y. H. Lee, W. Zhang, K. H. Wei and L. J. Li, *Adv. Mater*., 2013, **25**, 756.
6 M. S. Faber, R. Dziedzic, M. A. Lukowski, N. S. Kaiser, Q. Ding, and S. Jin. *J. Am. Chem. Soc*., 2014, **136**, 10053.
7 D. Voiry, H. Yamaguchi, J. Li, R. Silva, D. C. B. Alves, T. Fujita, M. Chen, T. Asefa, V. B. Shenoy, G. Eda and M. Chhowalla, *Nat. Mater*., 2013, **12**, 850.
8 D. Kong, H. Wang, Z. Lu, Y. Cui, *J. Am. Chem. Soc*., 2014, **136**, 4897.
9 V. Chakrapani, J. Thangala and M. K. Sunkara, *Int. J. Hydrogen Energy*, 2009, **34**, 9050.
10 W. F. Chen, K. Sasaki, C. Ma, A. I. Frenkel, N. Marinkovic, J. T. Muckerman, Y. Zhu and R. R. Adzic, *Angew. Chem., Int. Ed*., 2012, **51**, 6131.
11 Q. Liu, J. Tian, W. Cui, P. Jiang, N. Cheng, A. M. Asiri and X. Sun, *Angew. Chem. Int. Ed*., 2014, **53**, 6710.
12 P. Jiang, Q. Liu, Y. Liang, J. Tian, A. M. Asiri, and X. Sun, *Angew. Chem. Int. Ed*., 2014, **53**, 12855.
13 Y. Shi, Y. Xu, S. Zhuo, J. Zhang, and B. Zhang, *ACS Appl. Mater. Interfaces*, 2015, **7**, 2376.

14 J. M. McEnaney, J. C. Crompton, J. F. Callejas, E. J. Popczun, C. G. Read, N. S. Lewis and R. E. Schaak, *Chem. Commun.,* 2014, **50**, 11026.
15 W. F. Chen, C. H. Wang, K. Sasaki, N. Marinkovic, W. Xu, J. T. Muckerman, Y. Zhu and R. R. Adzic, *Energy Environ. Sci*., 2013, **6**, 943.
16 W. Chen, J. T. Muckerman and E. Fujita, *Chem. Commun*., 2013, **49**, 8896.
17 H. Vrubel and X. Hu, *Angew. Chem., Int. Ed*., 2012, **54**, 12703.
18 (a) Y. Feng, T. He and N. Alonso-Vante, *Electrochim. Acta*, 2009, **54**, 5252.
(b) D. Susac, L. Zhu, M. Teo, A. Sode, K. C. Wong, P. C.Wong, R. R. Parsons, D. Bizzotto, K. A. R. Mitchell and S. A. Campbell, *J. Phys. Chem. C*, 2007, **111**, 18715.
(c) L. Zhu, M. Teo, P. C. Wong, K. C. Wong, I. Narita, F. Ernst, K. A. R. Mitchell and S. A. Campbell, *Appl. Catal. A*, 2010, **386**, 157.
19 D. Kong, J. J. Cha, H. Wang, H. R. Leec and Y. Cui, *Energy Environ. Sci*., 2013, **6**, 3553
20 D. Wang, M. Gong, Hung. Chou, C. Pan, H. Chen, Y. Wu, M. Lin, M. Guan, J. Yang, C. Chen, Y. Wang, B. Hwang, C. Chen and H. Dai, *J. Am. Chem. Soc.*, 2015, **137**, 1587
21 (a) M. Muhler, W. Bensch and M. Schur, *J. Phys.: Condens Matter*., 1998, **10,** 2947.
(b) B. Gunnar and K. Arne, *Acta Chem. Scand.*, 1970, **24,** 1925.
22 M. Eagleson, *Concise Encyclopedia Chemistry*, Berlin: Walter de Gruyter, 1994, **1081**.
23 J. F.W. Mosselmans, R. A. D. Pattrick, G. van der Laan, J. M. Charnock, D. J. Vaughan, C. M. B. Henderson, C. D. Garner, *Phys. Chem. Minerals*, 1995, **22**, 311.
24 M. Basu, Z. W. Zhang, C. J. Chen, P. T. Chen, K. C. Yang, C. G. Ma, C.C. Lin, S. F. Hu, R. S. Liu, *Angew. Chem. Int. Ed*., 2015, **54**, 6211.
25 (a) J. K. Nørskov, F. Abild-Pedersen, F. Studt and T. Bligaard, Proc. *Natl. Acad. Sci*., 2011, **108**, 937.
(b) A. Vojvodic and J. K. Nørskov, *Science*, 2011, **334**, 1355.
26 J.O. Bockris and E.C. Potter, *J. Electrochem. Soc*., 1952, **99**, 169.
27 S. Trasatti, O. A. Petrii, *J. Electroanal. Chem*., 1992, **327**, 353.